International Journal of Solids and Structures 202 (2020) 368–383

Contents lists available at ScienceDirect

International Journal of Solids and Structures

journal homepage: www.elsevier.com/locate/ijsolstr

Bending induced wrinkling and creasing in axially crushed aluminum tubes

Jake A. Haley, Stelios Kyriakides *

Research Center for Mechanics of Solids, Structures & Materials, The University of Texas at Austin, ASE 5.230 Austin, TX 78712, USA

ARTICLE INFO

Article history:
Received 17 April 2020
Received in revised form 1 June 2020
Accepted 4 June 2020
Available online 27 June 2020

Keywords:
Crushing induced folding
Large compressive strain
Surface wrinkling
Crease formation

ABSTRACT

Concertina folding of tubes used for impact mitigation bends the tube section to tight curvatures that can lead to failures on the tensioned side of the folds. This paper reports results from such axial crushing experiments on Al-6061-T6 circular tubes in which cleft-like features were also observed on the compressed sides of folds. Microscopic examination of the compressed sides of sectioned folds at different stages of bending revealed the following. Compression leads to surface wrinkles that are initiated by small initial surface roughness. Further bending increases the amplitude of the wrinkles, and at even higher bending the wrinkles morph into folds, creases, and sharp discontinuities. Metallographic examination of these surface undulations revealed that surface wrinkles encompass several grains, which deform conforming to the imposed local geometric changes. With this in mind, the axial crushing was simulated at the continuum level via an axisymmetric finite element analysis coupled with a suitably calibrated non-quadratic elastic–plastic constitutive model. A sufficiently refined mesh and representative initial surface imperfections enabled monitoring of the evolution of surface instabilities on the compressed sides of folds. Surface wrinkles appear at compressive strains of about 50%. As the local bending increases, their amplitude grows, and subsequently they evolve into local folds, and creases that resemble surface features observed in the experiments.

1. Introduction

Compression of thin-walled inelastic structures leads to buckling instabilities, which tend to localize and can result in collapse and rupture. Wrinkling is an instability affecting the full thickness of a thin-walled structure like a circular tube in compression (e.g., see Bardi and Kyriakides, 2006) or bending(e.g., Corona et al., 2006) with a wavelength of order $\sqrt{Rt}$, where R and t are the radius and wall thickness of the shell. However, wrinkling can also manifest as a surface instability affecting only part of the wall and can develop both under compression and bending (e.g., see Triantafyllidis et al., 1982; Kuroda and Tvergaard, 2007). The latter surface instabilities do not possess a characteristic length and so they are excited by small surface imperfections and appear in a range of wavelengths. This paper discusses a problem that exhibits both structural and surface wrinkling instabilities, the axial crushing of an Al-alloy tube into concertina folding as shown in Fig. 1.

The tube shown has a relatively low D/t (25.5) so that the prevalent instabilities occur after the material enters the plastic range. Axial compression leads first to axisymmetric wrinkling with a well-defined wavelength (see Fig. 2 of Bardi and Kyriakides, 2006). The structure retains its load carrying capacity, but with continued compression the wrinkle amplitudes grow gradually decreasing its axial rigidity. Although more complicated scenarios are possible, in the simplest one of interest here, the progressive reduction of axial rigidity due to wrinkling results in a load maximum. Beyond this maximum the deformation localizes into one axisymmetric wrinkle. With further compression under displacement control, the amplitude of this wrinkle increases gradually evolving into a protruding lobe while the load drops as shown in the force–displacement response in Fig. 2. In the present experiments, the tubes were crushed between rigid platens as shown in Fig. 3. Due to the constraint provided by frictional contact between the ends and the platens, the first lobe occurred at one of the ends. As the lobe collapses, the end of the tube slides accommodating the folding of the wrinkle as shown in the cross-sectional view of the crushed tube in Fig. 1b. When the folded section makes self-contact, the load increases and a second fold starts to develop. A second load maximum is reached when the second fold starts to collapse. The load starts to rise again when the outer knee comes into contact with the first fold. With the load rising, a new inward

* Corresponding author.
E-mail address: skk@mail.utexas.edu (S. Kyriakides).

https://doi.org/10.1016/j.ijsolstr.2020.06.003
0020-7683/

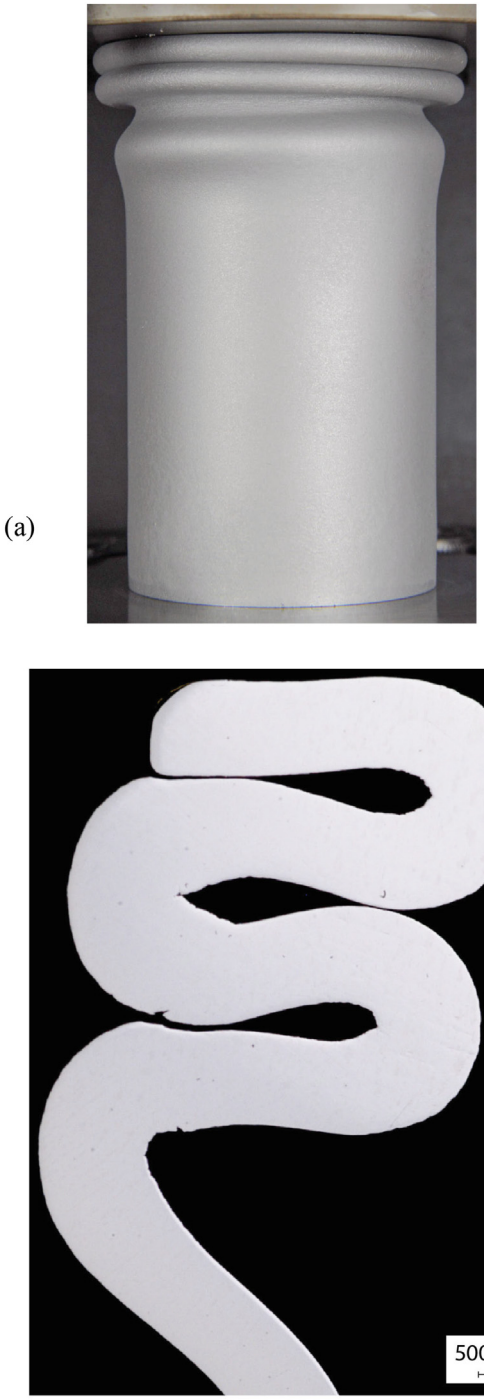

Fig. 1. (a) Crushed aluminum alloy tube exhibiting axisymmetric folding (Exp. II, $D/t = 25.6$). (b) Polished cross section of specimen in (a).

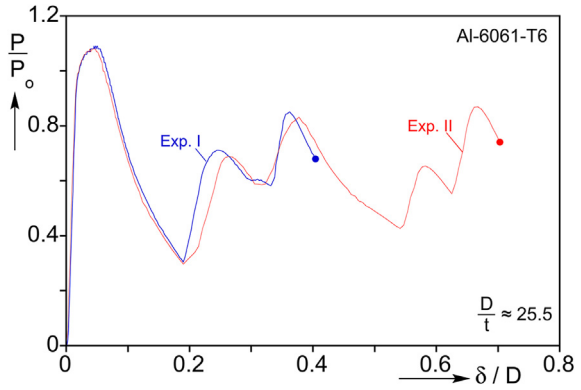

Fig. 2. Force-end displacement crushing responses recorded for Exps. I and II ($P_o = \pi(D-t)t\sigma_o$).

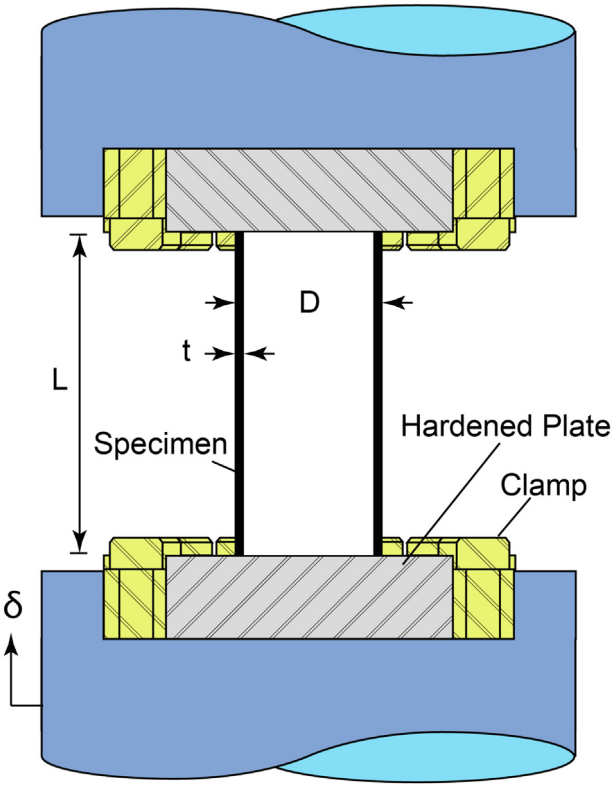

Fig. 3. The crushing tests were performed under displacement control using the setup shown schematically.

lobe starts to form and as it starts to collapse, a third load peak develops, and a new two-peak load cycle follows. The events described thus far are well known and well documented in the literature starting from the 1960s (e.g., see results in Bardi and Kyriakides (2003) and a brief review of the literature therein).

The main objective of the present study, was to detect tensile failures in tube crushing experiments and test the extent to which constitutive models and failure criteria developed for this alloy in Scales et al. (2019) and Chen et al. (2019) could track them. Indeed, tensile failures in at least two locations can be seen in the specimen cross section in Fig. 1b. At the same time, cleft-like features in the most bent sections on the compressed sides of the folds drew our attention. A more careful examination revealed in addition unexpected wrinkles, creases, and sharp discontinuities in these zones. This paper first presents grain level microscopic observations of these features at different stages of development, followed by a first attempt at reproducing them numerically.

2. Experimental

The experiments involved seamless extruded Al-6061-T6 tubes with the chemical composition given in Table 1. The test specimens were extracted from 12 ft (3.65 m) long, 2.0 in (51 mm) diameter mother tubes with a wall thickness of 0.187 in

Table 1
Al-6061-T6 chemical composition.

	Si	Fe	Cu	Mn	Mg	Cr	Zn	Ti	Al
Wt%	0.59	0.26	0.23	0.05	0.99	0.10	0.05	0.02	Bal.

(4.76 mm). The tubes crushed were about 4.3 in (110 mm) long. Close fitting solid inserts were placed inside the ends, and the outer surface was turned to the required wall thickness in a lathe such that the finished surface was concentric with the inner surface. The finished dimensions of the test specimens are listed in Table 2, where a small amount of residual wall eccentricity (Ξ_o) is reported. The stress–strain response of the material was measured using tension tests on full thickness axial test specimens extracted from the mother tubes and the yield stress σ_o is listed in Table 2.

The tubes were crushed between two rigid plattens in a servo-hydraulic testing machine under displacement control (see Fig. 3). The displacement rate was such that during the initial uniform deformation part of the test it resulted in a strain rate of $\dot{\varepsilon} \approx 2 \times 10^{-4}\ s^{-1}$. The force and displacement were recorded in a data acquisition system running LabView. The crushing of the specimen was monitored with time-lapse photography using a 12 MP digital camera running on a common time base with the data acquisition system. Typically, images were recorded at 8 s intervals. Post-processing related the images with the force displacement-response (typical such records are reported in Haley, 2020).

The crushed tubes were first examined externally and photographed intact as shown in Fig. 1a. This revealed a significant "orange-peel" type surface roughening on the outer surfaces of the folds. The tube was subsequently cut axially in half and the flat surfaces were polished for observation under a microscope. This produced images like the one in Fig. 1b in which some cracking on the outer surface is evident. Simultaneously, signs of winkles and crease-like features on the compressed side became apparent. This prompted a more detailed microscopic evaluation of specimens at magnifications at which the deformation at the grain level could be detected. To this end, sections were removed from one of the sectioned halves of the crushed tubes and polished followed by etching as described in Appendix A.

Images of the etched specimens were taken in a Keyence VHX-5000 digital microscope. The large field images were recorded at a magnification of 250× using 2-D auto-stitching with auto-focus in the microscope software. Each stitched image is captured at 1600 × 1200 pixel resolution. The assembled image is provided as a JPEG that can be as large as 20 k × 20 k pixels. The full image was then taken to Adobe Photoshop where brightness, color, and contrast were enhanced. The grain-level image of the section analyzed in the case of the tube from Exp. II is shown in Fig. 4. The high resolution of the full image (~11 k × 18 k pixels) allows one to zoom into parts of the section of interest. Thus for example, in Fig. 4 three areas of interest in yellow boxes will appear enlarged in subsequent figures.

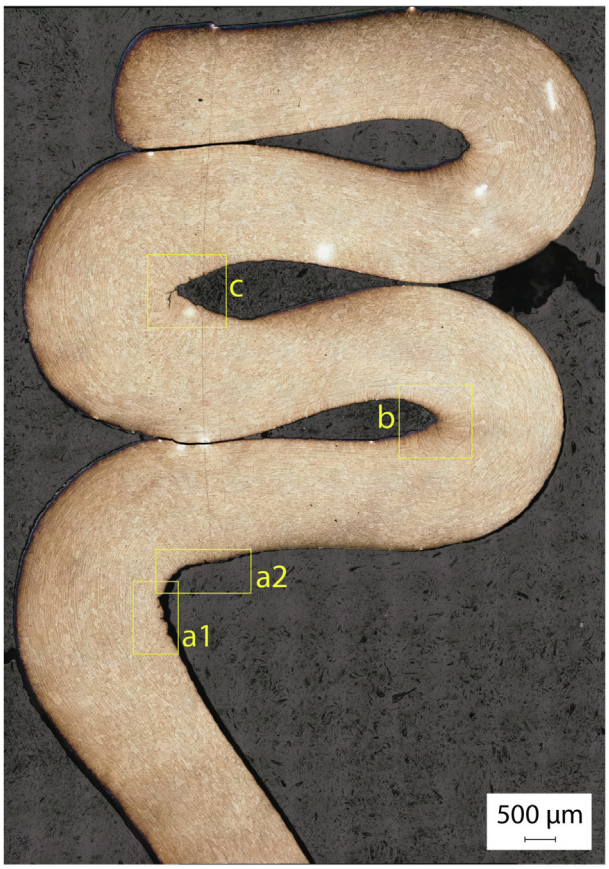

Fig. 4. Etched image of part of the cross section of the tube of Exp. II. Boxes identify areas of interest that appear subsequently enlarged.

The undeformed grain size distribution across the wall thickness of the mother tube was also established as a baseline for comparison with the deformation induced by the folds. A full thickness section removed from the mother tube was polished and etched as described in Appendix A. Fig. 5a shows an image of the whole cross section and Fig. 5b shows enlarged three zones: "a" is representative of the grain microstructure on the inner surface of the tube;

Table 2
Main parameters of crushed tubes analyzed.

Exp. No.	D in (mm)	t in (mm)	D/T and larger	L in (mm)	Ξ_o %	σ_o ksi (MPa)	δ_f in (mm)	Mode/Folds
I CR20	1.7666 (44.87)	0.0696 (1.769)	25.4	4.383 (111.3)	1.8	39.4 (273)	0.714 (18.14)	n0-1
II CR21	1.7655 (43.84)	0.0688 (1.748)	25.6	4.355 (110.6)	2.3	39.4 (273)	1.242 (31.55)	n0-2
III CR15	1.8265 (46.39)	0.0988 (2.510)	18.5	4.227 (107.4)	1.5	39.7 (274)	2.620 (66.55)	n0-3½
IV CR12	1.7240 (43.79)	0.0485 (1.232)	35.6	4.197 (106.6)	3.1	39.7 (274)	2.504 (63.6)	n0-2 n3-2

"b" represents the grain distribution away form the edges; and "c" is representative of the outer surface of the tube.

The distribution of grain size across the wall thickness (r-direction) and along the axial direction (x) was established using a type of *lineal intercept method* as described in ASTM E112-13, and the results are plotted in Fig. 6. What is apparent is that for the inner 70% of the wall thickness, the grain size is somewhat elongated along the axial direction but nearly uniform with an average size of about 70×100 μm. The grain sizes along the inner and outer surfaces are different. The inner surface starts with a zone about 200 μm wide with grain sizes representative of the interior, followed by a zone about 500 μm wide with grains that are significantly elongated along the axial direction. Similarly, elongated grains populate a zone about 700 μm wide along the outer surface, but here the finer grain zone at the edge is absent. These trends are also confirmed by the grain size plot in Fig. 6. It is worth remembering that the outer surface of all tubes discussed in this study was turned down in order to achieve the desired wall thickness. Consequently, their outer surface had the initial grain distribution representative of the central part of the wall thickness in "b". In addition, the enlarged images exhibit some fine lines along the axial direction. These are areas that underwent differential etching. They will also show up as deformed "stream lines" in the images of the folds that follow.

3. Experimental results

Results from four experiments involving tubes of different D/ts, crushed to different extents are presented (main parameters listed in Table 2). The analysis of the results concentrates on elucidating the evolution of surface instabilities on the compressed sides of the folds.

3.1. Experiment I

This involves a tube with a D/t of 25.4 crushed only to one complete axisymmetric fold as shown in Fig. 7a. The recorded force–displacement $(P-\delta)$ response is included in Fig. 2, and images of the deformed cross section are shown in Fig. 7b and c. The experiment was terminated just as an inward fold started collapsing while simultaneously an outward one started forming. This provides three zones of the cross section bent to different degrees marked in Fig. 7c. In zone "a," the inner surface is only lightly compressed by bending. In zone "b," the outer surface of the second fold is at a more advanced state of bending induced deformation, and zone "c" encompasses the compressed side of the competed fold. The three zones are shown expanded in Figs. 8a and 8b.

In zone "a" shown expanded in Fig. 8a, the microstructure, with the finer grain layer at the free edge and larger elongated grains somewhat further in, has deformed to accommodate the compression induced by the imposed curvature. The etching lines are also seen to follow the curvature of the section. Simultaneously, a significant number of surface undulations have appeared on the free surface. A total of 30 such wrinkles of varying amplitude have been identified with wavelengths ranging from about 50 μm to 240 μm with an average of 90 μm. A sub-zone of this image, designated as "a1," is shown expanded below image "a". Here the surface undulations are seen to consist of several grains of varying sizes, an indication that they are independent of the grain microstructure.

Fig. 8b shows expanded zone "b" together with subzone "b1" which zooms into the area with the largest curvature. Here because of the larger curvature of this fold, the grains are severely flattened to accommodate the local compression. The surface undulations are in a more advanced deformation state with significantly larger amplitudes. Because of the severity of the compression, several have morphed into folds, and interfaces of adjoining folds have become crevices or creases. Away from the free surface, the etching lines follow the induced curvature, whereas at the free surface they follow the deformation of the folds. The highly deformed grains inside the folds and the contours of the etching lines inside them indicate again that the formation of these folds and creases may be independent of the local microstructure.

Zone "c" in Fig. 8c shows the most compressed part of the completed structural fold. The large compression has caused the grains to flatten. Thus, the larger grains just inside the surface in Fig. 5b, in this micrograph are very elongated along the normal to the free surface. This elongation tends to decrease moving away from the free edge. The amplitudes of surface undulations at the top and bottom of the bent free surface increased significantly. Closer to the trough with the largest curvature, folds like the ones seen at site "b" in Fig. 8b, are now even more elongated, and adjoining creases are much deeper appearing as cracks. The local compression is so large that some of the folds are protruding out, breaking the continuity of the surface. One of the protruding folds is seen bent over its neighbors from which it is separated by a bifurcated crease.

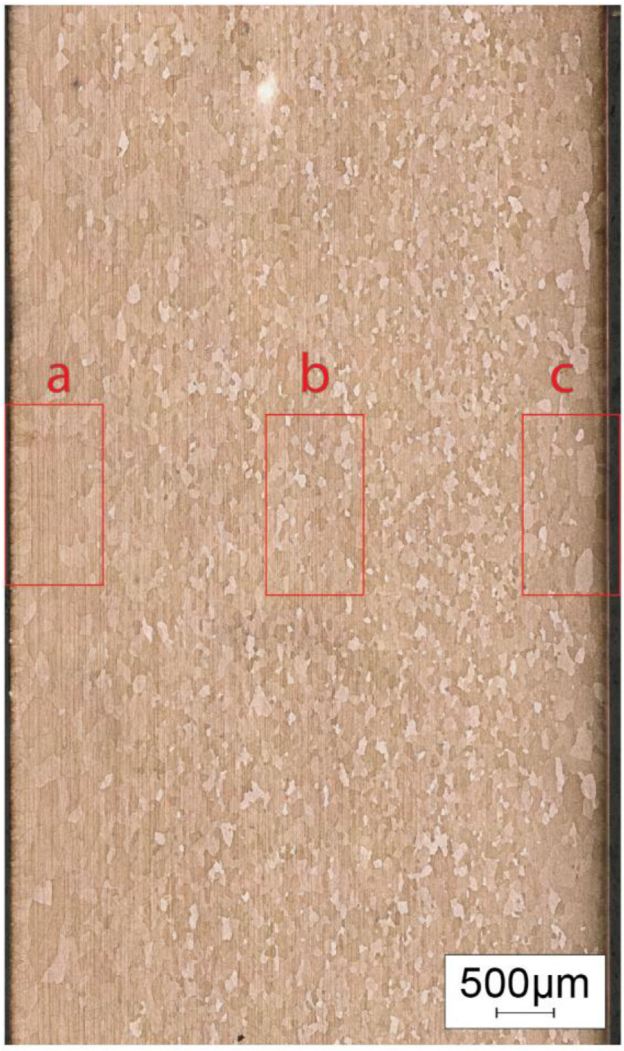

Fig. 5. Etched images showing the grain microstructure across the wall thickness of the undeformed extruded tube. (a) Full thickness – the left represents the inner surface. (b) Enlarged images showing grain distributions close to the inside surface "a," in the interior "b," and near the outer surface "c."

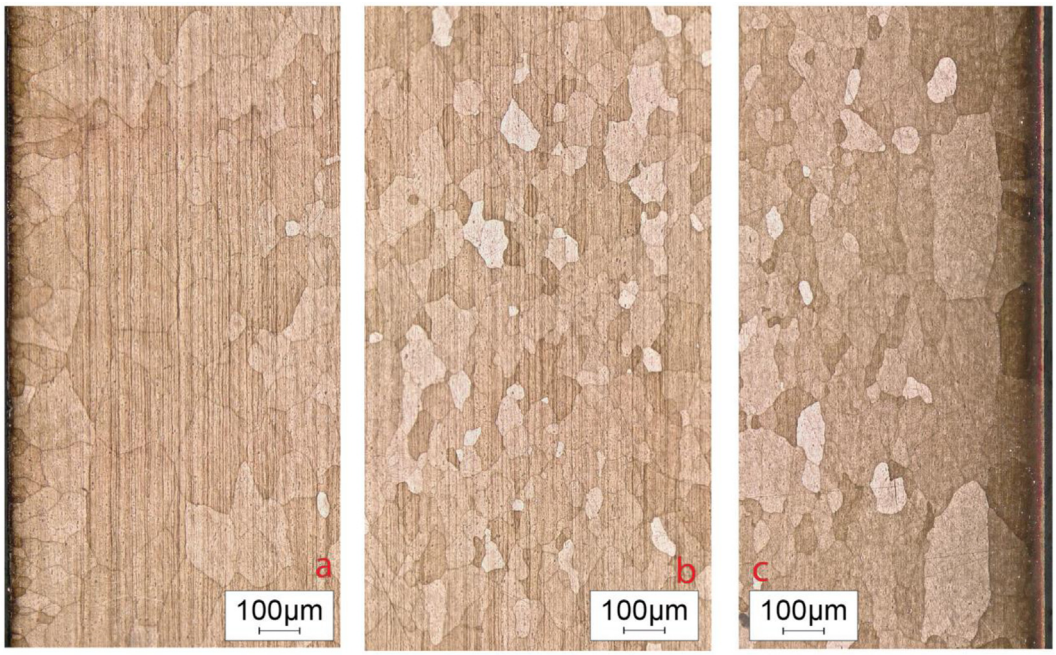

(b)

Fig. 5 (*continued*)

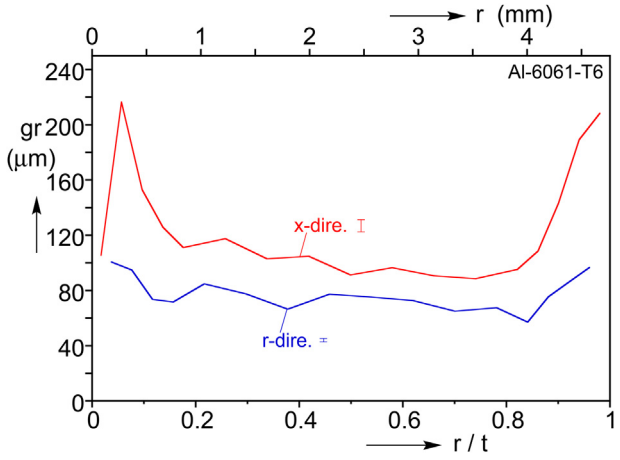

Fig. 6. Grain size measured across the tube thickness using a lineal intercept method; x is along the axis of the tube and r is a measure across the thickness starting from the inner surface.

Similar highly deformed surface folding, and the formations of clefts, creases and deep discontinuities have been observed in essentially all folds of the crushing experiments performed in this study, and prompted this more detailed investigation. Clearly, in any attempt to reverse bend such zones, the sharp clefts and creases will act at stress concentrations and lead to fracture (e.g., Das et al., 2001). This indeed confirms the empirical observation that when attempting to straighten a highly plastically bent metal rod or strip, it fractures. It is also worth mentioning that in the case of local dents or bends in larger structures (e.g., Kristoffersen et al., 2016), reverse bending imposed by springback can lead to fracture failures.

3.2. Experiment II

This experiment involves a tube with a similar D/t as the one of Exp. I, but it was crushed further forming two complete folds as shown in Fig. 1 (see Table 2). The force–displacement response recorded is included in Fig. 2 where it is seen to nearly replicate the response of Exp. I up to the point that experiment was terminated. The events associated with the crushing were outlined in the introduction. The crushing was terminated just as the second fold came into contact terminating local deformation and a third one started to form. The grain level micrograph of the affected part of the cross section is shown in Fig. 4. We are again mainly concerned with the compressed sides of the folds and have marked three areas for more detailed analysis.

Adjacent zones "a1" and "a2," shown expanded in Fig. 9a, come from the compressed outer surface of the lower partially bent lobe.

(a)

Fig. 7. (a) Crushed tube from Exp. I ($D/t = 25.6$). (b) Polished and etched cross sectional images from Exp. I. Boxes identify areas of interest that appear subsequently enlarged.

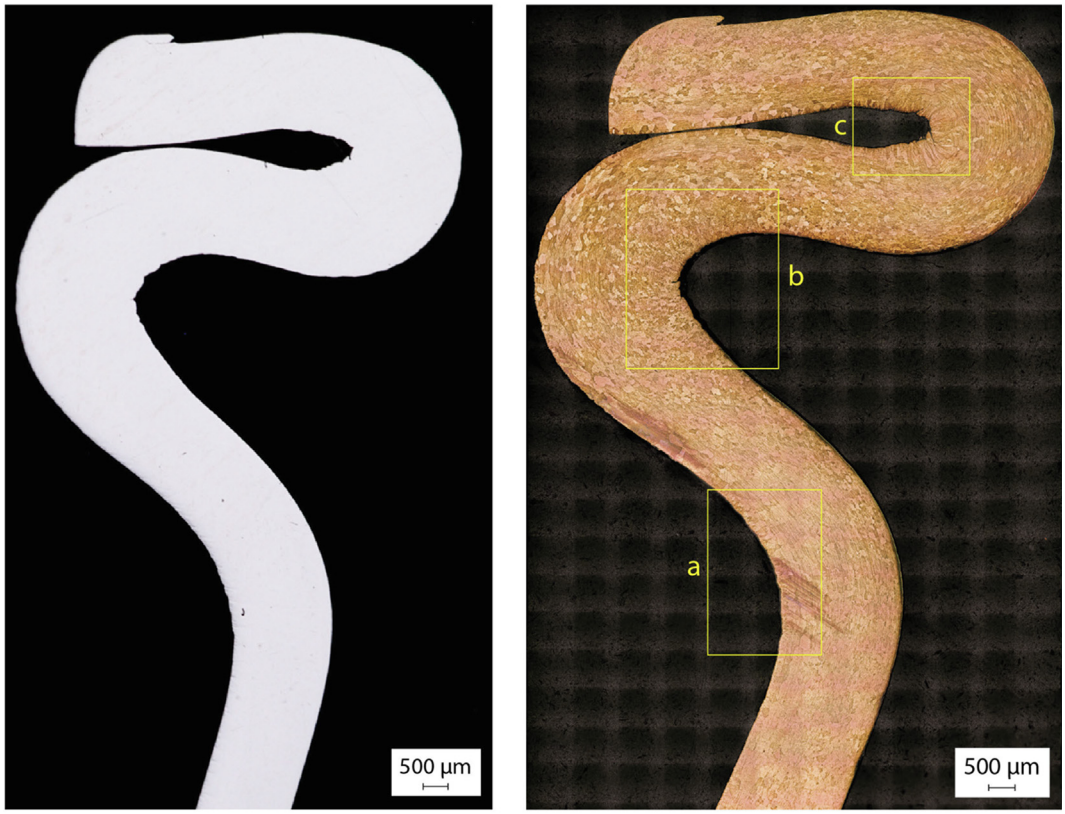

Fig. 7 (*continued*)

The surface of zone "a2" belongs to the end of the second fold and is not as severely bent as zone "a1." Its surface is covered by well-developed wrinkles with wavelengths ranging from about 85–160 μm. Moving to the left side of the image, the increasing curvature causes the amplitude of the local wrinkles to grow with several of them evolving into protruding folds separated by creases. Close to the free surface the etching lines follow the contours of the wrinkles but further in they follow that of the bent wall. Enlarging the image confirms that the wrinkles encompass several grains as reported earlier.

Zone "a1" is in the more bent part of this lobe and consequently several of the surface undulations have developed into protruding folds separated by crease-like depressions. Once again, these surface features encompass several highly deformed grains and the etch lines follow their surface contours. The grains just inside the free surface are highly elongated in along the normal to the surface. The etch lines exhibit some undulations consistent with differences in deformation in neighboring grains. They become smoother with their trajectories conforming to the imposed curvature further away from the free surface.

Zones "b" and "c" are shown expanded in Fig. 9b. Zone "b" shows the innermost section of the second fold and belongs to the inner surface of the tube. Several of the surface undulations have evolved into protruding folds separated by creases. Since this is an inner tube surface, the wrinkles and folds have finer grains on their surface with highly elongated large grains adjacent to them. These are the large grains close to the inner surface in the undeformed micrograph in Fig. 5b. They were originally longer along the axial direction, but here they are elongated in a direction normal to the free surface. One of the protruding folds has moved further out and is bent over its neighboring folds from which it is separated by a long crease. Overall, the observations are similar to those made for the image in Fig. 8c, which also involves an inner surface fold.

Zone "c" in Fig. 9b shows the most bent part of the trough formed between the first and second folds. The large local curvature has resulted in large amplitude wrinkles separated by creases. Several of the wrinkles are similar to those in image "a1." They encompass several highly deformed grains elongated along the normal to the free surface. The finer surface grains and the highly deformed inner grains in image "b" have been replaced by a more uniform grain microstructure consisting of highly deformed grains elongated along a direction normal to the free surface. On the surface of the wrinkles, the deformed grains conform to their rounded shapes. In the deepest part of the trough a protruding fold has bent over its neighboring ones, and this has formed a deep crease like feature.

The differences between the initial grain microstructure of the two surfaces of the tube influence to some degree the deformation inside the highly deformed fold. However, surface features like wrinkles, creases, and some of the sharper crevices are similar and appear to be driven by macroscopic material behavior.

3.3. Experiment III

This axial crushing experiment involved a tube with a D/t of 18.5 with the objective of investigating the effect of higher wall thickness on the surface instabilities of interest. The tube was crushed to three complete folds and the test was terminated with a fourth fold partially completed. Similar post-test analysis was performed on this specimen and only aspects that provide new information are presented here. Fig. 10a shows a full cross sectional view of the crushed tube, and Fig. 10b a partial image of the folded section that was polished and etched. An important

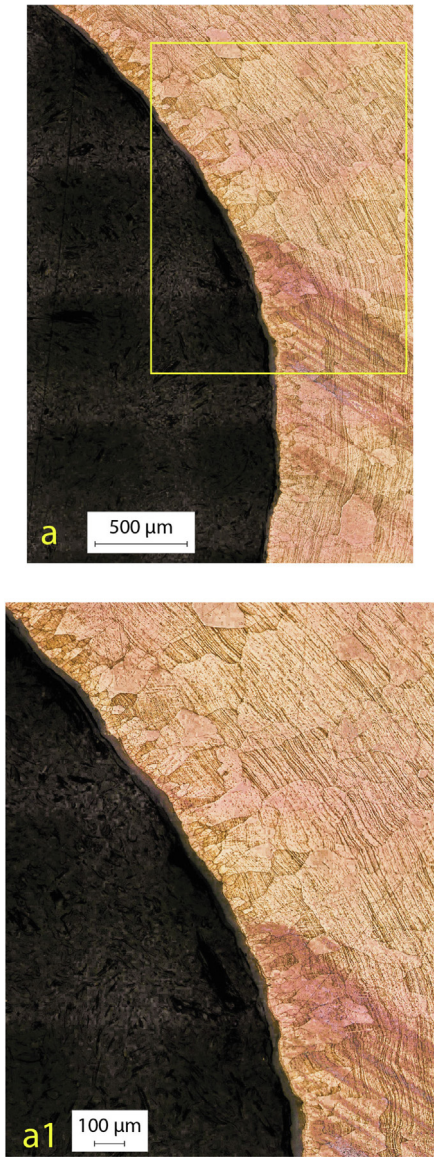

Fig. 8a. Expanded images of zones "a" and "a1" from the overall image in Fig. 7b that show surface wrinkles and grain deformation adjacent to it.

new development brought about by the increase in the wall thickness of the tube is that the inner extrados between the second-third and third-fourth folds have developed major ruptures. The global image in Fig. 10a shows the ruptures to affect the whole half circumference. It is interesting to observe that these ruptures occurred at the same locations on the folds as in the higher D/t tube in Fig. 1b, but those failures had just initiated.

The most deformed zones of the folds were analyzed and the observations are in concert with those presented thus far. The surface instabilities in troughs associated with the inner surface of the tube, resemble those in Figs. 8c and 9b-"b", and those that originated from the outer surface of the tube resemble those in Fig. 9b-"c". Thus an image of the boxed zone in Fig. 10b is relegated to Appendix B.

The tube crushed in a nearly axisymmetric fashion, but this does not necessarily imply that the surface instabilities do not vary around the circumference. The confocal feature of the Keyence VHX-5000 digital microscope was used to further investigate this issue. The zone examined comes from the partially deformed fourth fold in Fig. 10a (marked with a red box). A 20-degree sector was removed from the crushed tube and the section of interest was placed on the microscope stage with the trough normal to the microscope. A 3-D image is captured by first defining the in-plane $(x-y)$ bounds of the scan. The out of plane (z) coordinates of the depth of the scan are then established ensuring that the highest and lowest parts are within focus. The depth of the presented scan was 2800 μm and the confocal feature captured an image in the z-direction every 14 μm. The 3-D image generated is shown in Fig. 11, it covers a circular arc of about 8 degrees.

The surface wrinkles are clearly discernible in the trough of the bent section, where they impart an uneven, rough appearance to the bent surface. The wrinkle wavelengths are consistent with the values reported for Exps. I and II. The wrinkles are separated by discontinuities, which can be seen on the cross section to be crease like. They generally follow the circular profile of the circumference of the fold, but some of the wrinkles and creases tend to deviate from the circumferential trajectories presumably because of microstructural or other obstacles. This indicates that the locations of wrinkles, folds and creases observed on any axial section of a crushed tube can differ from those on another axial section. However, overall this three-dimensional view supports the observations made from the 2-D images.

A fourth experiment is included in Table 2 with $D/t = 35.6$. In this case crushing resulted in two-axisymmetric folds followed by two mode-3 folds. Despite the much thinner wall thickness, the compressed side of both types of folds exhibited similar surface wrinkling, accompanied in the most highly bent zones by creases and clefts. At the same time, no ruptures were observed on the tensioned sides, which points to the expected role of wall thickness on tensile failures.

3.4. Review of surface wrinkling/creasing under compression in metals

Surface wrinkling under compression in elastomers and generally soft materials has received very significant attention in the literature starting with Biot (1963). In the solid mechanics community, creasing appears to have been first reported by Gent and Cho (1999) from a simple bending test on a soft rubber block. More recently, both surface wrinkling and creasing have received renewed attention due to interest in materials like gels, foams, and biological materials as a mechanism for the development folds–gyri (e.g., Hong et al., 2009; Hohlfeld and Mahadevan, 2011; Cao and Hutchinson, 2012). The literature on the subject is too vast and its review is beyond the scope here where the focus is on surface instabilities in metals.

In contrast to soft materials, surface instabilities in compressed metal structures have received scant attention presumably because they appear at rather large strains. The few experimental references we have identified deal mainly with thin-walled structures bent to tight curvatures. For example, the *bendability* of sheet metals is typically determined in a three-point bending test in which a strip is bent into a v-shape using indenters with radiused tips (e.g., Davidkov et al., 2012; Mattei et al., 2013). An alternative is the wrap-bend test where the sheet is bent around a radiused surface by a tool (e.g., Lloyd et al., 2002; Shi et al., 2016a; Muhammad et al., 2019a). By using parts of increasingly smaller radius, the aim is to establish the smallest radius that the tensioned side can be bent to without cracking, an issue of particular importance to hemming but also in other sheet metal forming processes. These tests, in conjunction with simulations using crystal plasticity, have been used to evaluate the effect of various alloys and processing combinations on the bendability of Al-alloy sheets. The main concern in these bending studies has been tensile failures, which render a part unusable. Consequently, information on what happens on the compressed side has been very limited. However, careful examination of some of the published images of bent

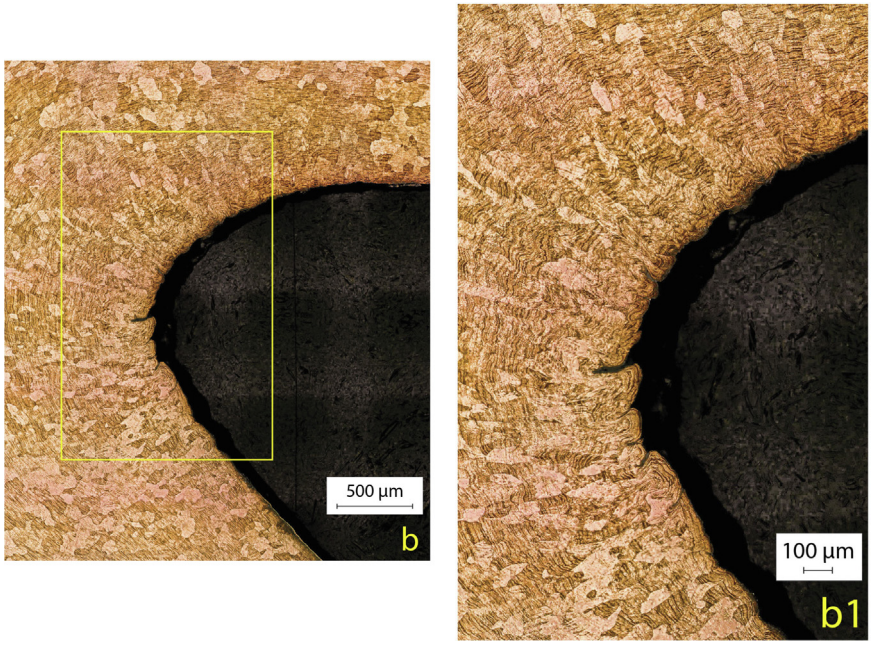

Fig. 8b. Expanded images of zones "b" and "b1" from the overall image in Fig. 7b. The larger curvature of this zone caused the amplitudes of surface undulations to grow with several of them separated by creases. Observe also the large distortion of the grains adjacent to the surface.

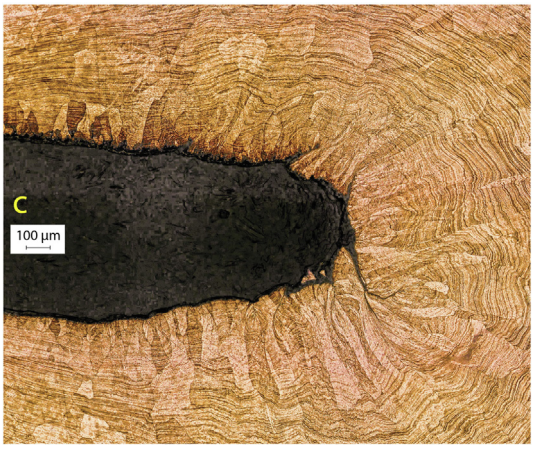

Fig. 8c. Expanded image of zone "c" showing the inner surface of the completed fold in Fig. 7b. The very tight local curvature caused several of the undulations to protrude outward with several of them separated by deep crevices. The grains adjacent to the surface are highly flattened along the normal to the surface to accommodate induced compression.

parts show signs of surface instabilities on the compressed sides. Examples include Fig. 6 of Muhammad et al. (2019a) that involved bending of a clad aluminum alloy sheet, Figs. 5, 7, and 9 of Mattei et al. (2013), and Fig. 1b of Shi et al. (2016b). The most direct reference to surface instabilities and "cracks" on the compressed side of a bent surface of an AA6000 series sheet is made in a brief proceedings manuscript by Li and Wu (2007). Their micrographs in Fig. 3 show these features, as well as very elongated grains adjacent to them that are similar to those in Figs. 8c and 9b.

Surface instabilities have also been reported by Kristoffersen et al. (2016) on the concave side of a transverse dent induced in a 142 mm diameter X-65 tube. The tube had a D/t of 25.4 and was indented by a transverse indenter with 10 mm radius in a three-point bending set up (see Fig. 4 of ref.). Deep dents were introduced to tubes both quasi statically as well by impact. The three-point loading bent the tubes in an overall manner but also produced transverse dents as much as 380 mm wide. In one of the troughs of the dents, wrinkles were observed with wavelengths of the order of 120 mm. The wrinkles are well developed and are separated by crease-like features (see Fig. 12 of ref.).

Surface wrinkling and folding with adjacent crevices has also been reported to occur in tribology studies involving a hard wedge sliding against a metal surface (Mahato et al., 2014, 2017). The highly compressed zone ahead of the wedge develops wrinkles that evolve into folds separated by crease-like features.

The formation and evolution of surface instabilities under plane pure bending in an elastic–plastic plate was studied by Triantafyllidis et al. (1982). The corner theory of plasticity was used to bend a hardening material plate with sinusoidal surface imperfections. The amplitudes of surface undulations grow particularly on the compressed side and lead primarily to shear banding on the tensioned side. Bending was further studied by Kuroda and Tvergaard (2004, 2007) using periodic sectors with surface imperfections and plasticity models capable of capturing the evolution of texture, including crystal plasticity. In these works the emphasis was on shear banding on the tensioned side. Thus, although the growth of wrinkles on the compressed side was observed, the periodic geometry adopted did not allow the localization of wrinkling that might occur at higher curvatures.

Crystal plasticity has also been used to simulate experiments performed to determine the bendability of sheet metal. For example, Muhammad et al. (2019b) simulated wrap-bend tests on clad Al-alloy sheets. Their results show the effectiveness of cladding in preventing or delaying shear band failures. Here also, the compressed side was of limited interest.

Recently Yang et al. (2019) analyzed the growth of a crease in a metal block under plane strain compression. The material is a J_2 elastic–plastic solid with linear hardening. A small cusp-like imperfection in the form of two 90° circular arcs is introduced, and the growth of the base of the cusp in monitored as the block is compressed. It is demonstrated that the depth of the crease tends to increase sharply at global strains of the order of −0.5. Increasing the hardening slope tends to decrease the "critical"

Fig. 9a. Expanded images of zones "a1" and "a2" from the overall image of tube from Exp. II in Fig. 4. Part of zone "a2" that is less bent shows surface wrinkles, whereas the more bent left side shows more pronounced wrinkles separated by creases. The higher curvature of zone "a1" has caused more significant protruding undulations and creasing.

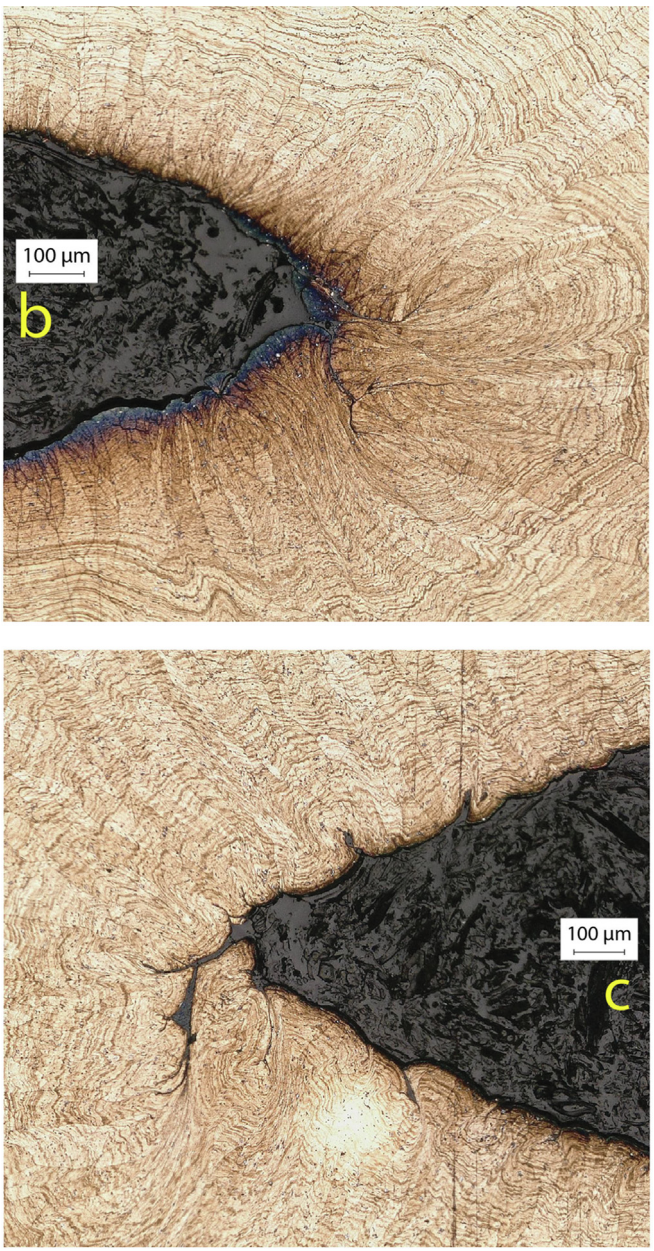

Fig. 9b. Expanded image of zones "b" and "c" showing the most deformed parts of the troughs of the completed folds in Fig. 4. The very tight local curvatures caused several of the undulation to protrude outward while being separated from adjacent ones by deep crevices. Observe the somewhat different grain deformation adjacent to the surfaces of the inner- and outer-oriented folds.

strain whereas for hardening levels representative of metals the "critical" strain is larger than −0.8.

4. Simulation of axisymmetric tube crushing

In this first attempt to simulate the evolution of surface instabilities observed in our tube crushing experiments, we examine the problem in a simplified axisymmetric setting. We adopt the geometry and mechanical properties of the tube of Exp. I in Table 2, and simulate numerically the crushing of the first couple of folding cycles. The calculation is performed in ABAQUS 6.13/Standard using mainly axisymmetric elements CGAX4R with reduced integration. The model is crushed between two rigid planes. To capture the expected surface undulations, a fine mesh is adopted on the outer surfaces of the tube while the inner 75% of the wall thickness is meshed more coarsely.

The model tube has an overall length of 4.383 in (111 mm) and is divided into three sections as shown in Fig. 12. The calculations are large so we chose to capture the evolution of surface instabilities as the second fold develops. For that reason the finer mesh, shown expanded in Fig. 12, is assigned only to the section that is affected by the second fold of length $L_2 = 0.656$ in (16.7 mm). The outer layers of width $t_1 = 0.0086$ in (218 μm) are meshed with 16 elements with nearly 1:1 aspect ratio with sides of approxi-

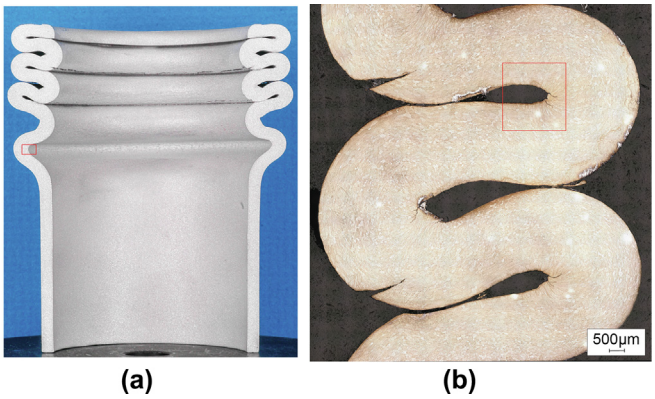

Fig. 10. (a) Cross section of crushed tube with D/t = 18.5 from Exp. III. (b) Polished and etched image showing part of the folded cross sectional image. Observe the significant failures on the tensioned sided of the inner folds.

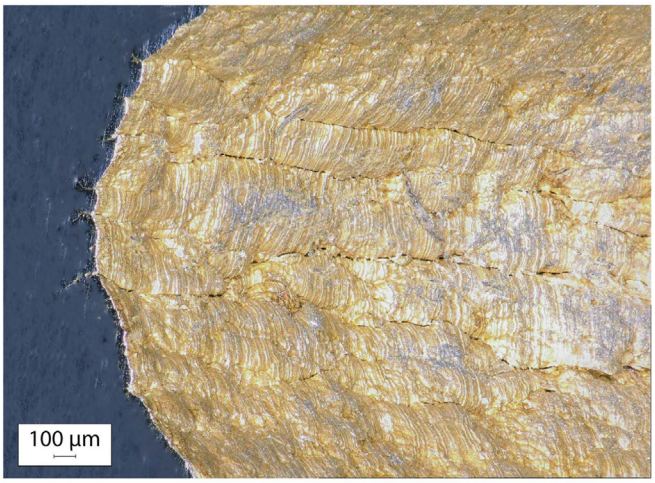

Fig. 11. Three-dimensional rendering of the inner surface of the third fold from Exp. III obtained using a confocal microscope (location marked in Fig. 10a). Observed are surface undulations separated by creases on the inner surface of the fold that trace azimuthal directions. The depth of several crease-like features can be seen on the cut surface on the left.

mately 0.54×10^{-3} in (13.7 μm). The interior has twelve elements of the same height. The upper section of length $L_1 = 0.868$ in (22.0 mm) is meshed with four elements across the thickness with a nearly 1:1 aspect ratio, which are sufficient to capture the folding with the required accuracy. The simulation of the inward folding of the top part of the model was particularly challenging because of the significant sliding and large deformation that the contacting surface undergoes. The contact of the top surface with the rigid plane was frictional using a friction coefficient of 0.25 and an exponential pressure-overclosure softening relationship. At the lower end, a length of $L_1 = 2.859$ in (72.6 mm) is also meshed with four elements across the thickness. The contact with the lower rigid surface is frictionless.

The surface roughness measured on the inner surface of the tubes used in the crushing experiments shown in Fig. C1a is assigned as an imperfection to the inner surface of the finer mesh middle section. The imperfection was replicated to cover the whole length L_2 and was introduced by shifting the surface nodes to match the measured profile. The imperfection amplitude dies exponentially, becoming zero at the mid-thickness.

The material is modeled as an elastic–plastic solid using the non-quadratic anisotropic yield function Yld04-3D of Barlat et al. (2005). This model with an exponent of 8 was calibrated using tubes from the same batch as those used in the crushing experiments in Chen et al. (2019). The determined constants are listed in Table 3 – see reference for more details. In the same work the constitutive model was shown to perform well in simulations of localization type instabilities. The stress–strain response of the material was measured in a uniaxial tension test on an axial specimen cut from one of the mother tubes used in the experiments. The specimen necked at a strain of about 7% so the measured force–elongation response was used to extrapolate the hardening response to a strain of 37% following the inverse procedure of Tardif and Kyriakides (2012) together with the Yld04-3D yield function. Fig. 13 shows the resultant stress–strain response where for higher strains a Voce extrapolation was adopted.

4.1. Numerical results

The calculated force-end shortening response $(P/P_o - \delta/D)$ is plotted in Fig. 14a. The tube crushes in the manner outlined for the experiment in Section 1. Compression causes localization into a protruding lobe at the top; its amplitude grows with the overall load dropping and evolves into a fold with part of the top surface folding inwards. This folding traces the two-peak response that follows the first load valley. A third load peak is reached indicating the formation of a second fold. A more detailed description of the folding is given in Section 2.3.1 and Section 4.2.1 of Haley (2020). Here we pick up the events associated with the formation of the second fold during the last descending part of the response. Fig. 14b shows a set of cross-sectional images of the model with the lower part of L_3 truncated for clarity. The color contours superimposed on the images represent the strain level. The images correspond to the stations marked on the response in Fig. 14a with numbered bullets.

We are particularly interested in the evolution of surface undulations in the intrados of this fold. Thus the section of the tube between the red lines marked in the images has been assigned the refined mesh (length L_2). The imperfection has been introduced to the inner surface of this section (left side of mesh in Fig. 12). With the load decreasing, a ⊃ shaped section is gradually folding so that by image 10 its upper side is about to contact the first fold, at which time the load will start increasing again. In the process, the inner surface of the lower intrados is undergoing significant compression imposed by the increasingly larger local curvature.

We have chosen to expand the most deformed part of this intrados, contained in the box drawn in red on each image in Fig. 14b. The box has a constant size and is placed at nearly the center of the zone of the most bent section. Fig. 15 shows the evolution of this zone in going from deformed configurations 1–10. For better clarity, the expanded images are presented as follows: Fig. 15a 1–4, Fig. 15b 6–8, and Fig. 15c 9–10. The color represents the strain level.

In configuration 1 in Fig. 14b, the local curvature is relatively small, but the surface strain is still of the order of 0.50. This level of strain is reflected in the elongation of the elements along the normal to the free surface close to it in image 1 in Fig. 15a. The compression is sufficient to excite the imperfections in the zone of interest, resulting in the appearance of small amplitude undulations on the surface. In image 2, the larger local curvature increases the compressive strain to about 0.65 and the amplitude of the surface undulations has increased further with signs of localization of some of the undulations appearing. With further increase in the local curvature in configuration 3, some of the surface undulations in image 3 appear as creases at early stages of development. In image 4, where the surface strain is of the order of 0.85, the amplitude of surface undulations has grown further, and two of the surface depressions have “folded” into creases. In images 5 and 6, the

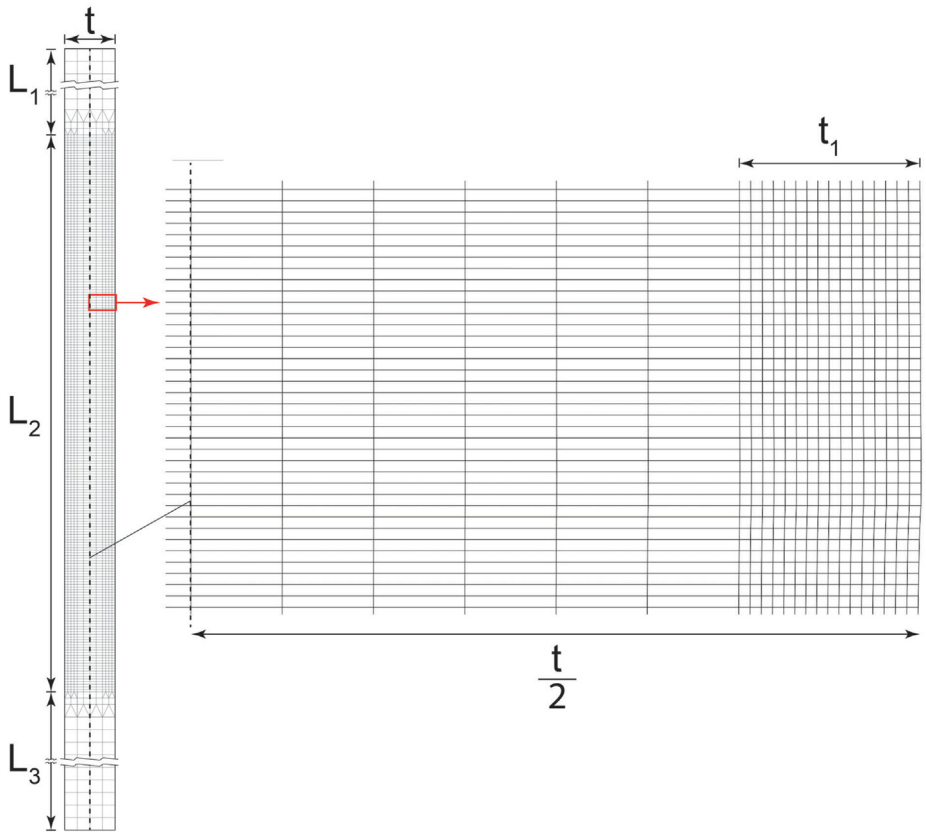

Fig. 12. The geometry and mesh of the axisymmetric finite element model used to simulate tube crushing.

Table 3
Anisotropy parameters for Yld04-3D yield function (Chen et al. 2019).

c'_{12}	c'_{13}	c'_{21}	c'_{23}	c'_{31}	c'_{32}	c'_{44}	c'_{55}	c'_{66}
1.028	1.150	1.162	0.941	0.679	0.985	1.0	1.0	1.367
c''_{12}	c''_{13}	c''_{21}	c''_{23}	c''_{31}	c''_{32}	c''_{44}	c''_{55}	c''_{66}
0.713	0.683	0.847	1.093	1.056	0.962	1.0	1.0	0.695

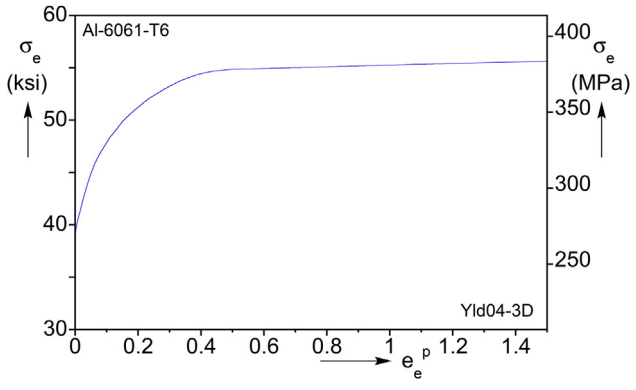

Fig. 13. The stress-plastic strain response of Al-6061-T6 used in the analysis.

additional increase in the local curvature causes the amplitude of surface undulations to grow, leading to local folding and deepening of the creases, and concurrently new crease-like features appear. Note also the additional elongation of elements close to the surface along its normal direction. The growth of surface undulations, the increase in the folding, and deepening of creases continues in images 7 and 8, where the strain now exceeds 1.0. It is worth noting that the strain around the highly deformed surface features is much higher. Although at this stage we have probably reached the limits of our discretization scheme – several elements in the folded up zones are highly distorted – we include images 9 and 10. Here the local undulations are even more deformed, the creases much deeper, and the strains in the folds and creases are of the order of 1.50. The calculation was terminated at station 10.

Overall, despite the simplified axisymmetric setting of our numerical simulation, and the neglect of any microstructural effects, the compressed intrados of the model exhibit surface undulations that are similar to those seen in the experiments. For bending induced compressive strain levels of about 0.50, the imperfection introduced to the surface excites surface wrinkling. As the curvature increases, the wrinkles multiply, their amplitude grows and they morph into crease-like folds. At even higher curvatures, the amplitudes of the folds grow and the creases deepen.

We consider this to be a first attempt at simulating the significant folding and creasing induced by the large curvatures imposed by the crushing of Al-6061-T6 tubes, which must be followed by more extensive studies. We can however, report the following from our limited parametric study of the problem.

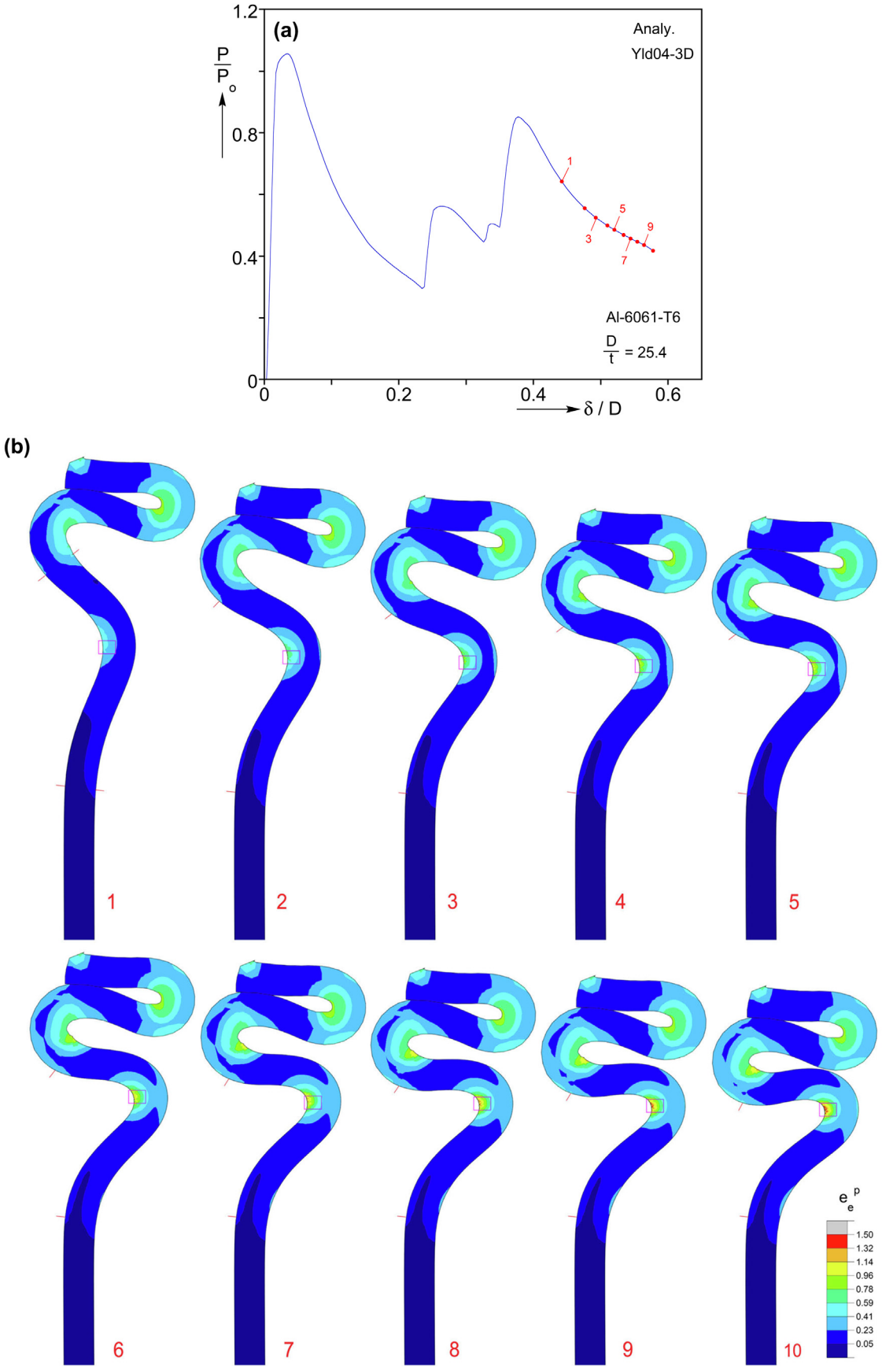

Fig. 14. (a) Calculated force-end displacement crushing response. (b) Global configurations corresponding the formation of the second fold corresponding to the stations marked on the response in (a) with numbered bullets.

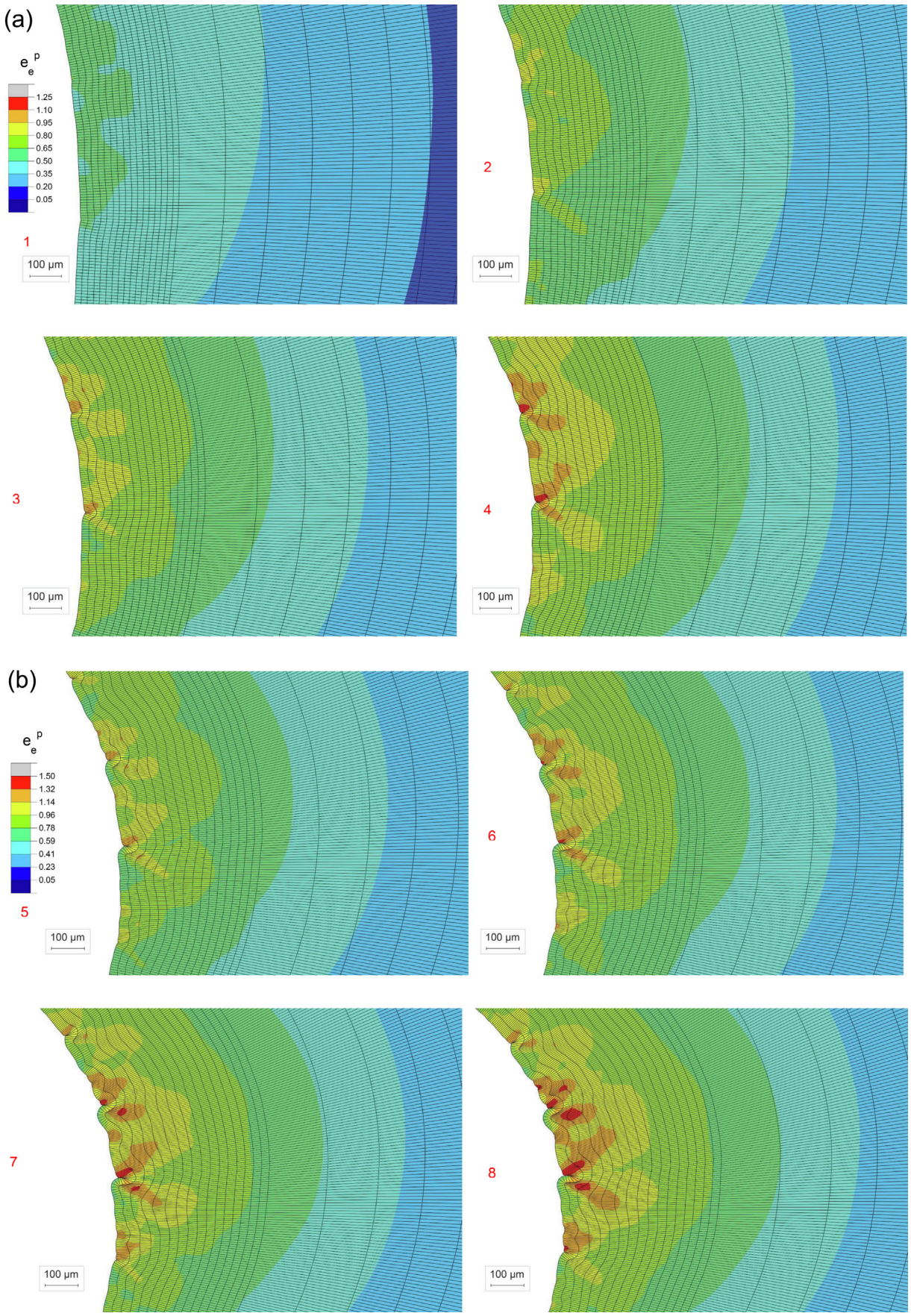

Fig. 15. Expanded images of zone is red box in Fig. 14b that show the evolution of surface undulations. (a) Images 1–4, (b) images 5–8 and (c) images 8–10.

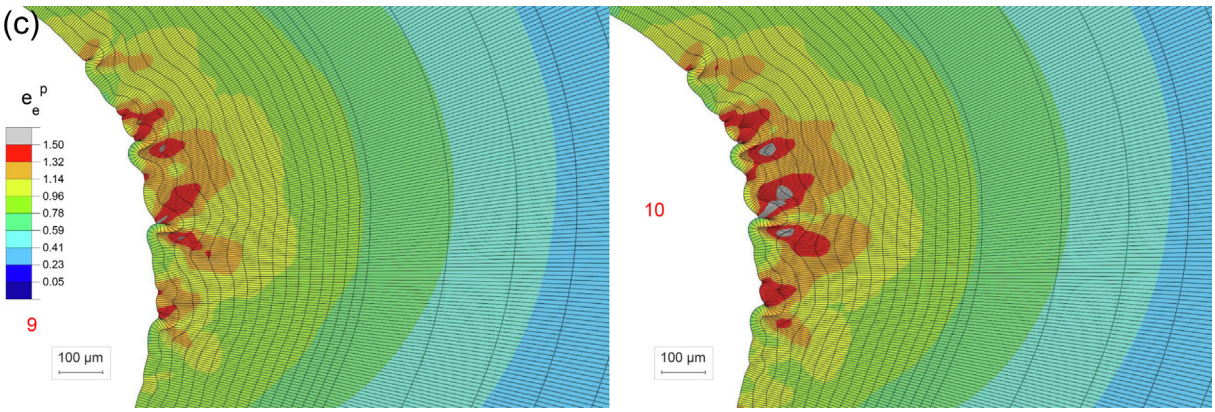

Fig. 15 (*continued*)

a. The evolution of the observed surface instabilities is influenced by the amplitude of the imperfections imposed to the surface of the tube crushed. Reducing the amplitude to one-half resulted in similar surface patterns, however their growth was delayed; to reach similar levels of deformation as in Fig. 15 required larger curvature.
b. In the simulation presented, an imperfection that mimics the initial surface roughness of the inner surface of our extruded tubes was adopted. However, similar surface instabilities were observed for other imperfections such as the sinusoidal on used in Triantafyllidis et al. (1982).
c. Similar results were obtained when the Yld04-3D anisotropic yield function was replaced by its isotropic version with the same exponent of 8 – i.e., Hosford (1972) non-quadratic yield function.
d. Tracking the further deepening of creasing requires improvements to the model such as adoption of improved contact algorithms and more appropriate meshing. Adoption of crystal plasticity will clearly add more clarity about the interaction of continuum level and microstructural events.
e. The evolution of surface instabilities on the tensioned parts of the folds generated by crushing has been studied widely by previous researchers and we purposely avoided repetition. However, we point out that a more conventional model of crushing in Haley (2020) reports tensile strain levels high enough to cause local tearing at the extrados of inner folds where rupture is observed in the experiments (e.g., see Fgis. 1b and 10).

5. Concluding remarks

We have been investigating failures in crushed Al-alloys tubes used for impact mitigation in the automotive and other industries. Concertina folding leads to tensile failures and tearing. Unexpected cleft-like features were observed on the compressed sides of folds also. Careful microscopic examination of these zones revealed that bending-induced compression leads first to surface wrinkling. Additional bending increases the amplitude of the wrinkles, and with further bending the surface wrinkles morph into folds, creases, and sharp discontinuities. In any attempt to reverse bend such zones, the sharp clefts and creases are bound to result in catastrophic fracture of the section. In the case of local dents and bends in large structures, unloading due to springback may be sufficient to lead to local fracture.

Metallographic examination of the concertina folds revealed that surface wrinkles encompass several grains, which deform conforming to the imposed local geometric changes. This implies that this surface instability is mainly governed by continuum level kinematics. The grain deformation continues to conform to the growth of the wrinkles into folds and at the early stages of creasing. As the creases deepen and develop into clefts, the highly deformed microstructure appears to interact more strongly with these surface features.

Although some variation of these features was observed around the circumference of concertina folds, the surface instabilities are fairly close to being axisymmetric. Consequently, in the first attempt at simulating the surface instabilities using continuum mechanics presented, the tube crushing was idealized as axisymmetric and was discretized with finite elements. The elastic–plastic behavior of the Al-alloy is represented using a non-quadratic anisotropic constitutive model shown in previous studies to capture well localization type instabilities. The model successfully simulates the crushing of a tube used in the experiments into the first two folds. The analysis enabled monitoring of the evolution of surface instabilities on the intrados of the second fold. This part of the model was discretized with a fine enough mesh, and small surface imperfections were introduced on the compressed side to prime the surface instabilities. As the local strain reaches a level of about 50%, surface wrinkles develop and their amplitude grows as the local bending increases. With additional bending the wrinkles evolve into local folds and creases that resemble surface features observed in the experiments. Although the strain level as which these surface features occur are quite large, they can be dangerous in structures that undergo significant bending due to local denting and/or other off-design loadings.

Intellectual property

We confirm that we have given due consideration to the protection of intellectual property associated with this work and that there are no impediments to publication, including the timing of publication, with respect to intellectual property. In so doing we confirm that we have followed the regulations of our institutions concerning intellectual property.

Declaration of Competing Interest

The authors declare that they have no known competing financial interests or personal relationships that could have appeared to influence the work reported in this paper.

Acknowledgements

The authors acknowledge with thanks financial support received for this work from the United States National Science

Foundation through the GOALI grant CMMI-1663269. The literature on failure under bending induced tension is vast, so the cited references are limited to those we have found useful in our study.

Appendix A

Metallographic analysis

Sections of the crushed specimens containing the folds were molded in an epoxy puck and ground down starting with 320-grit size sand paper and progressively moved down to 1200-grit size. The sample was then polished using cloth pads with progressively finer polishing diamond suspensions. This started with 3 μm particles in a water lubricant, followed by a 1 μm diamond suspension, and finished a 0.05 μm colloidal silica suspension slurry.

The specimens were then etched by fully submerging the pucks, first in a 1.33% aqueous solution of sodium hydroxide for about 90–120 s, and then in Weck's alkaline solution (2.67% potassium permanganate + 0.67% sodium hydroxide) for about 30 s, to obtain a better contrast between microstructural features. This is a somewhat modified formula to the one of Weck and Leistner (1996), established by trial and error to result in cleaner etching particularly at inside and outer the surfaces of the sectioned specimen.

Appendix B

Experiment III micrograph

Fig. B1 shows an expanded image of the most deformed zone of the second fold of the crushed tube of Exp. III, identified with a box in Fig. 10b. The zone shows the trough involving the inner surface of the tube, and it thus exhibits similar surface features to those observed in Figs. 8c and 9b-"b" from the higher D/t experiments. These included surface wrinkles with highly compressed small grains near the surface, highly elongated larger grains adjacent to them flattened by compression, and several protruding folds separated by creases and crevices.

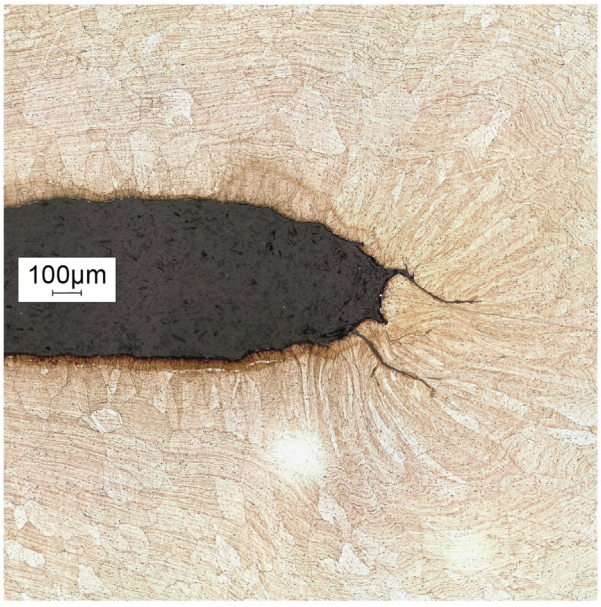

Fig. B1. Expanded image of the boxed zone in the larger image of the crushed section of the tube of Exp. III in Fig. 10b.

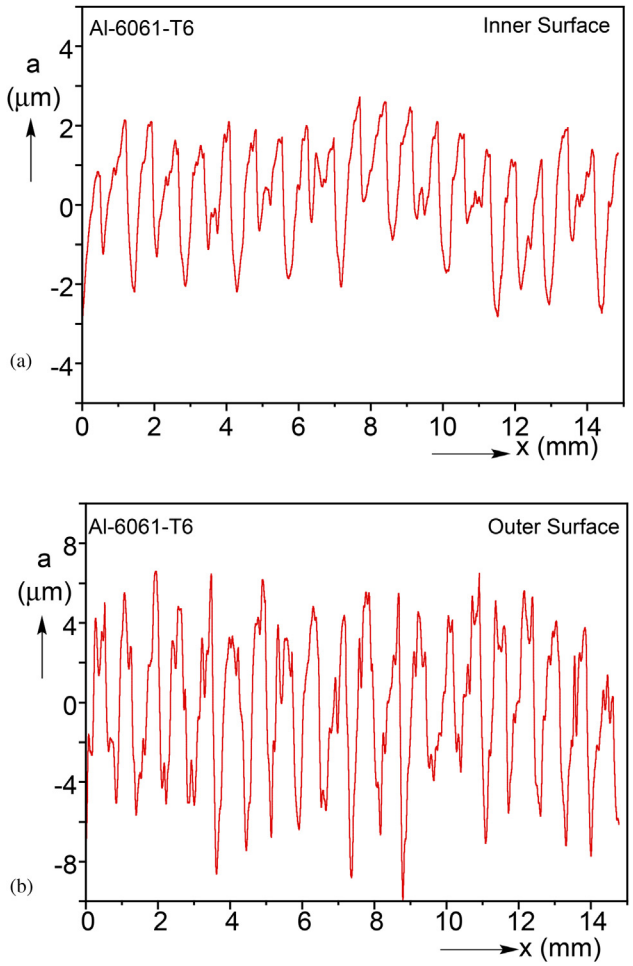

Fig. C1. Axial scans of initial surface roughness of tubes used in the experiments. (a) Inner surface, and (b) outer machined surface.

Appendix C

Surface roughness

The surface roughness in the axial direction of the tube of both the inside (as received) and outside (machined) surface of the tube was measured using a Keyence vHX-5000 digital microscope. A magnification of 250x and a vertical pitch of 2 μm in the 3-D profile measurement (confocal) function of the microscope produced the surface profiles in Fig. C1. Both surfaces exhibit rather regular nearly periodic profiles. Interestingly, despite the difference in their origin, the wavelengths of surface undulations for both surfaces range between 400 and 800 μm with an average of 600 μm. However, the maximum amplitudes for the outer surface are about 7 μm and for the inner close to 2 μm.

References

Bardi, F.C., Kyriakides, S., 2003. On the axisymmetric progressive crushing of circular tubes under axial compression. Int'l J. Solids Struct. 40, 3137–3155. https://doi.org/10.1016/S0020-7683(03)00111-2.

Bardi, F.C., Kyriakides, S., 2006. Plastic buckling of circular tubes under axial compression—part I: experiments. Int'l J. Mech. Sci. 48, 830–841. https://doi.org/10.1016/j.ijmecsci.2006.03.005.

Barlat, F., Aretz, H., Yoon, J.W., Karabin, M.E., Brem, J.C., Dick, R.E., 2005. Linear transformation-based anisotropic yield functions. Int'l J. Plast. 21, 1009–1039. https://doi.org/10.1016/j.ijplas.2004.06.004.

Biot, M.A., 1963. Surface instability of rubber in compression. Appl. Sci. Res. Sect. A 12, 168–182.

Cao, Y., Hutchinson, J.W., 2012. From wrinkles to creases in elastomers: the instability and imperfection-sensitivity of wrinkling. Proc. R. Soc. A 468, 94–115. https://doi.org/10.1098/rspa.2011.0384.

Chen, K., Scales, M., Kyriakides, S., 2019. Material response, localization, and failure of an aluminum alloy under combined shear and tension: Part II Analysis. Int'l J. Plast. 129, 361–379. https://doi.org/10.1016/j.ijplas.2019.04.002.

Corona, E., Lee, L.-H., Kyriakides, S., 2006. Yield anisotropy effects on buckling of circular tubes under bending. Int'l J. Solids Struct. 43, 7099–7118. https://doi.org/10.1016/j.ijsolstr.2006.03.005.

Das, S., Chen, J.J.R., Murray, D.W., Wilkie, S.A., Zhou, Z.J., 2001. Wrinkle behavior under cyclic strain reversal in NPS12 pipe. In: Proc. 20th Int'l Conf. Offshore Mechanics Arctic Eng., OMAE2011/PIPE-4011.

Davidkov, A., Jain, M.K., Petrov, R.H., Wilkinson, D.S., Mishra, R.K., 2012. Strain localization and damage development during bending of Al–Mg alloy sheets. Mater. Sci. Eng. A 550, 395–407. https://doi.org/10.1016/j.msea.2012.04.093.

Gent, A.N., Cho, I.S., 1999. Surface instabilities in compressed or bent rubber blocks. Rubber Chem. Tech. 72, 253–262. https://doi.org/10.5254/1.3538798.

Haley, J.A., 2020. On the axial crushing and failure of aluminum alloy tubes: experiments and numerical simulations M.S. Thesis. Engineering Mechanics, University of Texas, Austin.

Hohlfeld, E., Mahadevan, L., 2011. Unfolding of sulcus. Phys. Rev. Lett. 106, 10502. https://doi.org/10.1103/PhysRevLett.106.105702.

Hong, W., Zhao, X., Suo, Z., 2009. Formation of crease on the surface of elastomers and gels. Appl. Phys. Lett. 95, 11091. https://doi.org/10.1063/1.3211917.

Hosford, W.F., 1972. A generalized isotropic yield criterion. ASME J. Appl. Mech. 39, 607–609. https://doi.org/10.1115/1.3422732.

Kristoffersen, M., Borvik, T., Langseth, M., Hopperstad, O.S., 2016. Dynamic versus quasi-static loading of X65 offshore steel pipes. Eur. Phys. J. Spec. Top. 225, 325–334. https://doi.org/10.1140/epjst/e2016-02629-4.

Kuroda, M., Tvergaard, V., 2004. Shear band development in anisotropic bent specimens. Euro. J. Mech. – A/Solids 23, 811–821. https://doi.org/10.1016/j.euromechsol.2004.05.006.

Kuroda, M., Tvergaard, V., 2007. Effects of texture on shear band formation in plane strain tension/compression and bending. Int'l J. Plast. 23, 244–272. https://doi.org/10.1016/j.ijplas.2006.03.014.

Li, Z., Wu, X., 2007. Inner surface cracking of an aluminum alloy in small-radius bending. In: Proc. ASME Int'l Mech. Eng. Cong. Expo.. https://doi.org/10.1115/IMECE2007-42976.

Lloyd, D., Evans, D., Pelow, C., Nolan, P., Jain, M., 2002. Bending in aluminium alloys AA 6111 and AA 5754 using the cantilever bend test. Mater. Sci. Technol. 18, 621–628. https://doi.org/10.1179/026708302225003604.

Mahato, A., Guo, Y., Sundaram, N.K., Chandrasekar, S., 2014. Surface folding in metals: a mechanism for delamination wear in sliding. Proc. R. Soc. A 470, 20140297. https://doi.org/10.1098/rspa.2014.0297.

Mahato, A., Ho, Y., Guo, Y., Viswanathan, K., Sundaram, N.K., Udupa, A., Mann, J.B., Chandrasekar, S., 2017. Sinuous flow and folding in metals: implications for delamination wear and surface phenomena in sliding and cutting. Wear 376–377, 1534–1541. https://doi.org/10.1016/j.wear.2017.02.012.

Mattei, L., Daniel, D., Guiglionda, G., Ocker, H., Driver, J., 2013. Strain localization and damage mechanisms during bending of AA6016 sheet. Mater. Sci. Eng. A 559, 812–821. https://doi.org/10.1016/j.msea.2012.09.028.

Muhammad, W., Kang, J., Brahme, A., Ali, U., Hirsch, J., Brinkman, H., Engler, O., Mishra, R., Inal, K., 2019a. Bendability enhancement of an age-hardenable aluminum alloy: Part I — relationship between microstructure, plastic deformation and fracture. Mater. Sci. Eng. A 753, 179–191. https://doi.org/10.1016/j.msea.2019.03.053.

Muhammad, W., Brahme, A., Ali, U., Hirsch, J., Engler, O., Aretz, H., Kang, J., Mishra, R., Inal, K., 2019b. Bendability enhancement of an age-hardenable aluminum alloy: Part II – multiscale numerical modeling of shear banding and fracture. Mater. Sci. Eng. A 754, 161–177. https://doi.org/10.1016/j.msea.2019.03.050.

Scales, M., Chen, K., Kyriakides, S., 2019. Material response, localization, and failure of an aluminum alloy under combined shear and tension: Part I Experiments. Int'l J. Plast. 129, 340–360. https://doi.org/10.1016/j.ijplas.2019.04.004.

Shi, Y., Jin, H., Wu, P.D., Lloyd, D.J., 2016a. On the study of sheet bendability in AA5754-O temper alloy. Metall. Mater. Trans. A 47, 5203–5213. https://doi.org/10.1007/s11661-016-3658-5.

Shi, Y., Zhao, P., Jin, H., Wu, P.D., Lloyd, D.J., 2016b. Analysis of surface roughening in AA6111 automotive sheet under pure bending. Metall. Mater. Trans. A 47, 949–960. https://doi.org/10.1007/s11661-015-3260-2.

Tardif, N., Kyriakides, S., 2012. Determination of anisotropy and material hardening for aluminum sheet metal. Int'l J. Solids Struct. 49, 3496–3506. https://doi.org/10.1016/j.ijsolstr.2012.01.011.

Triantafyllidis, N., Needleman, A., Tvergaard, V., 1982. On the development of shear bands in pure bending. Int'l J. Solids Struct. 18, 121–138. https://doi.org/10.1016/0020-7683(82)90021-X.

Weck, E., Leistner, E., 1996. Metallographische Anleitung zum Farbätzen nach dem Tauchverfahren Teil III: Nichteisenmetalle, Hartmetalle und Eisenwerkstoffe, Nickel-Basisund Kobalt-Basis-Legierungen, Series of Specialist Books on Welding Technology Band 77/III.

Yang, J., Jin, L., Hutchinson, J.W., Suo, Z., 2019. Plasticity retards the formation of creases. J. Mech. Phys. Solids 123, 305–314. https://doi.org/10.1016/j.jmps.2018.08.016.